Kimiabeigi M, Widmer JD, Baker NJ, Martin R, Mecrow BC, Michaelides A.
Three-Dimensional Modelling of Demagnetization and Utilization of Poorer Magnet Materials for EV/HEV Applications.
***IEEE Transactions on Energy Conversion* 2016, 31(3), 981-992.**

3D Modelling of Demagnetization and Utilization of Poorer Magnet Materials for EV/ HEV Applications

M. Kimiabeigi, J. D. Widmer, N. Baker, R. Martin, B. Mecrow, *Member, IEEE*, and A. Michaelides

***Abstract*—High performance electric motor designs with ferrite magnets have recently gained interest due to the high and volatile price of rare earth magnets. However, due to the relatively poor coercivity of ferrite magnets, these designs are highly susceptible to demagnetization, as a result of which accurate modelling and better understanding of this phenomenon is particularly important. In this paper, the impact of the motor stack length and level of magnetic saturation on the demagnetization risk are studied based on 3-Dimensional Finite Element (3D FE) simulations and a proposed lumped circuit model. It is shown that reducing the stack length can significantly enhance the demagnetization resistance, with the effect being more pronounced for designs with a higher level of magnetic saturation. To benchmark the practicality of the concept, a previously presented high performance ferrite based design is modified by using a 30% weaker grade of ferrite magnet whilst shortening the stack length. It is shown that the demagnetization withstand capability of the design was significantly enhanced and exceeded the short circuit requirement with a good safety margin. The theoretical findings have been supported by prototype testing.**

***Index Terms*—Demagnetization, Electric Vehicle (EV), Ferrite Magnets, Finite Element (FE), Hybrid Electric Vehicle (HEV), 3-Dimensuional Effects (3D).**

I. Introduction

Permanent magnet (PM) motors are amongst the best candidates for applications where high power density and energy efficiency are required, such as electric and hybrid-electric vehicle (EV and HEV) applications [1]-[4]. However, to limit the very high back electromotive force (BEMF) at high speed operations, the flux linkage due to permanent magnets needs to be weakened by injecting an appropriate amount of armature current in the negative direct axis (d-axis) position [5]. As the negative d-axis field opposes the permanent magnet field, the magnets are exposed to a risk of demagnetization, the severity of which depends on the characteristics of the magnetic circuit as well as the magnets' intrinsic coercivity, H_{cj}, [6]. A more critical situation can occur during the short circuit faults, where negative d-axis currents with much larger amplitude than the peak inverter current can develop, [7].

Due to their high remanent flux density, B_r, and high H_{cj}, the rare earth magnets, such as Neodymium Iron Boron (NdFeB), are excellent candidates that may contribute to high power density applications, while experiencing a minimal risk of demagnetization. However, due to the high and rather volatile price of the rare earth elements during the last decade, research toward using cheaper grade of magnets, such as NdFeB with less Dysprosium (Dy) contents, or ferrite magnets has, recently, become popular, [8], [9]. One of the major challenges with these designs is to mitigate the risk of demagnetization by appropriate modelling and optimization of the magnetic circuit path, which may be achieved by approaches such as: a) using interior permanent magnet topologies (IPM), b) providing leakage path for the demagnetization flux, by tapering the flux barriers toward the airgap [10], or allocating non-magnetic void on top [11] or both top and bottom [12] of the magnets, c) thickening the magnets width in the direction of magnetization, [9], [12], and d) increasing the number of poles [12].

Due to complexity of modelling, most of the papers have only studied the 2-dimensional (2D) demagnetization behavior [6], [7], [10], [13], [14]. In this respect, some have used Finite Element models to identify and mitigate the demagnetization risk by optimization of the design topology [10], [14], whilst others have used fast analytical techniques to diagnose and prevent demagnetization during the motor operation, [6], [7], [13]. 3D FE studies have tended to focus on end winding leakage calculations, for example [15], [16], and have provided accurate analytical expressions which may be incorporated into the 2D equivalent circuit of an electrical machine. Even though, several papers such as [15], [17], [18], analytically, or [19], numerically (using FE), have derived and described the impact of 3D parameters on the performance of electrical machines, their modelling is often limited to derivations of airgap flux density, BEMF and torque, while the 3D effect of the stack length variation on the demagnetization

The project is funded by Innovate UK under Grant 110130.

M. Kimiabeigi, J. Widmer, N. Baker, R. Martin, and B. Mecrow are with Newcastle University, NE17RU, UK (mohammad.kimiabeigi@ncl.ac.uk); A. Michaelides is with Jaguar Land Rover, Gaydon, UK.

performance has not been, explicitly, addressed.

In this paper, the 3D effects of the stack length on the demagnetization are, for the first time, investigated. The investigation has been made using 3D FE (assuming non-linear materials), which is performed on a high power density spoke type ferrite motor, the design details of which have been previously presented in [12], [20]. A lumped magnetic circuit model is derived and used to explain the observations from the 3D FE, based on the variation of the magnet load line against the circuit parameters. Using the proposed model, the effects of the stack length and the magnetic saturation are decomposed and explained. The practicality of the concept is benchmarked by comparing two grades of ferrite magnets (one with 30% lower H_{cj} than the other) in terms of demagnetization resistance and the static torque performance.

The novelty of this paper can be addressed in the following areas:

a) This paper for the first time identifies and explains an important relation between the stack length and the permanent magnets demagnetization performance within an electrical machine application.

b) Following a detailed proof and explanation of the phenomenon, which has been a source of deviation between the prototype testing and simulation results in the previous disclosures [12], [20], the concept is, further, viewed as a potential measure to exploit cheaper grade of magnets for high performance low cost traction motor applications. On this basis, some first principle design assessments and validations for both low power (HEV) and high power (EV) designs have been provided.

c) Finally, the 3D concept has been formulized using a simple but practical reluctance based coefficient in Section VI, which can be incorporated into any existing design optimization program and result in more accurate estimation of the demagnetization behavior, thereby achieving cheaper but higher performing motor designs.

II. Original EV Motor Design and Motivation for Study

The original topology and specifications of the electric motor analyzed in this paper result from a project funded by the UK funding agency Innovate UK. This project's objective is to design a low cost, but high performance, electric drive for use in a battery electric vehicle. Some of the major project requirements and data are summarized in Table I. Based on multi-physics optimizations, a spoke type design with a distributed winding (slots per pole and phase equal to 2) and using FB9B grade magnets has been developed; a one-tenth model of the optimal design, applying half axial symmetry, and including only two coils belonging to one of the phases is shown in Fig. 1. Furthermore, the key geometrical dimensions are addressed in Table II.

TABLE I
DESIGN REQUIREMENTS FOR THE FERRITE BASED TRACTION MOTOR.

Available volume (cylinder)	< 14 liter
Peak power density per motor volume	>6 kW/liter
Continuous power density per motor volume	>4 kW/liter
Base to top speed ratio	3000 rpm : 15000 rpm
Maximum winding temperature	180 ˚C
Available water cooling options	Only via outer stator frame
Demagnetization withstand capability	3-phase short circuit
Maximum achievable inverter current, $I_{pk\text{-}3\ phase}$	420 Arms
Minimum available DC link voltage	400 V
FB9B Ferrite, B_r at 20˚C/ H_{cj} at 20˚C	0.44 T/ 370 kA/m
Ceramic 8 Ferrite, B_r at 20˚C/ H_{cj} at 20˚C	0.38 T/ 260 kA/m

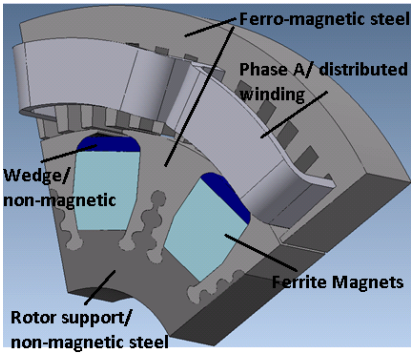

Fig. 1. 3D model of the reference motor design, with one-tenth of the original length.

TABLE II
Major dimensions of the spoke type design.

Stator outer diameter (mm)	205
Rotor outer diameter (mm)	140
Stack length (mm)	195
Airgap (mm)	0.5

To simplify early prototype build and test set-up, a prototype with same 2D profile but one-fifth of the stack length has been constructed. During test it was observed that the demagnetization withstand capability of the short length prototype is significantly better than the 2D FE predictions (which assume an infinitely long machine). As a result, to validate the 3D effects on demagnetization, and due to the significant improvements observed due to these effects, an in-depth 3D analysis of the disclosed ferrite motor design, Fig 1 and Table II, has been performed in the present paper. It was intended that this study would improve understanding of demagnetization in ferrite based motor designs as this is one of the major obstacles in their use for traction application [21].

III. Influence of Stack Length on Demagnetization

A. 3D FE modelling

To quantify the effect of the stack length on demagnetization performance of the design described in Section II, a large current (400% of the peak inverter current, I_{pk}, Table I) has been injected in the negative d-axis position, and the stack length has been varied from the design value of 195 mm to 39 mm (1/5th axial length). The field strength, H, observed in the magnets for a number of differing stack lengths was studied, and the results are shown in Fig 2. The red areas are those where the H field is greater than the intrinsic coercivity of the FB9B grade Ferrite magnet at 20˚C,

and therefore complete demagnetization may be expected. Furthermore, to better understand the end effects the demagnetization at both the end face, i.e. the face closest to the end windings, and the middle stack face, i.e. the face farthest from the end windings, are simulated and both shown in Fig. 2. It should be noted the choice of 400% I_{pk} as the basis for analysis, which is much larger than the simulated three phase short circuit current of 160% I_{pk}, [12], is partly to improve the visibility of the comparisons (which, also, includes, the study of the effects due to magnetic saturation), and partly to address the more severe conditions such as asymmetric single phase short circuits, [7].

From Fig. 2, it can be observed that the field strength inside the magnets is significantly reduced as the stack length decreases. Whilst for the 195 mm stack length design, a significant portion of the magnets is at risk of full or partial demagnetization, for the 39 mm stack length the risk is reduced to zero. Furthermore, on the end face the circumferential edges of the magnets are always at risk of demagnetization, almost regardless of the stack length of the design; however, as the axial depth of the end face demagnetized region is very limited (about 1 mm), this region will not have a noticeable impact on the overall performance. Finally, it should be noted that the 3D FE results converge to 2D FE predictions for, relatively, long stack lengths, in this case the 3x39 mm stack length and beyond.

The phenomenon in Fig. 2 can be partly explained due to the 3D variation of the magnetic reluctance, and partly based on the magnetic saturation effects; both of these effects are addressed analytically in Section III.B. To support the analytical modelling, the flux vectors and flux density in different regions of the 3D model have been plotted (for different stack length models and different current amplitudes) and shown for the 39 mm stack model in Fig 3. As can be seen for the periodic 2-pole model in Fig 3, during 3-phase short circuit conditions (corresponding to 160% peak inverter current) a significant portion of the armature field results in slot leakage (indicated as slot leakage flux in Fig. 3) and therefore does not reach and endanger the magnets in the rotor. However, some portion of the armature field (illustrated as demagnetizing flux in Fig. 3) passes the airgap and influences the rotor, including the pole tips and non-magnetic regions on top and bottom of the magnets. This field has the potential to cross and reverse the polarity of some parts of the magnets, leading to demagnetization.

The path of the demagnetizing flux is indicated in Fig 3. To better assess the reluctance of the stator and airgap (to be used in Section III.B for analytical modelling), the flux density in the most flux concentrated region of the yoke (located in the middle of the critical yoke edge in Fig 3(b)) and in the airgap, (identified as the critical point in the airgap in Fig 3(a)), are calculated and compared for 39 mm and 3x39 mm stack lengths in Figs. 4 and 5. As can be seen in Figs. 4 and 5, for low levels of demagnetizing currents i.e. when saturation is negligible, shortening the stack length results in the increase of the flux density in both the stator and the airgap. The source and implication of this phenomenon are discussed in Appendix I.

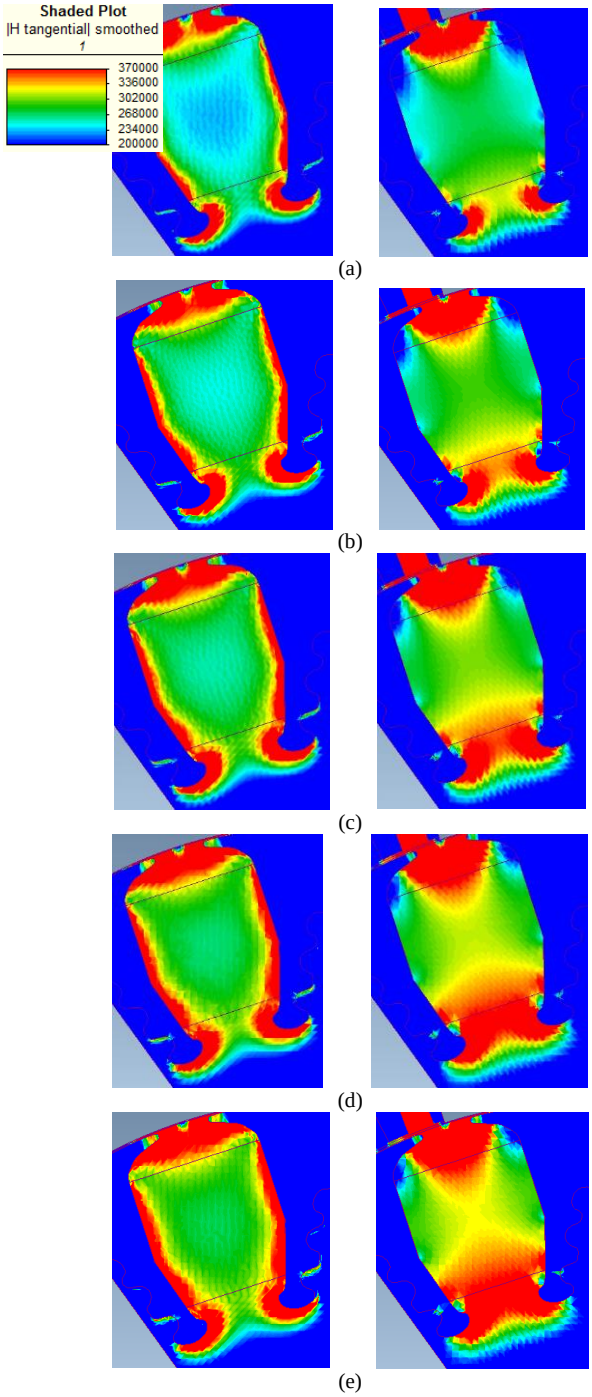

Fig. 2. H distribution in the FB9B magnets, 400% I_{pk}, models with different stack lengths. (a) 39 mm. (b) 49 mm. (c) 59 mm. (d) 3x39 mm. (e) 5x39 mm. Left column: end faces. Right column: middle stack faces.

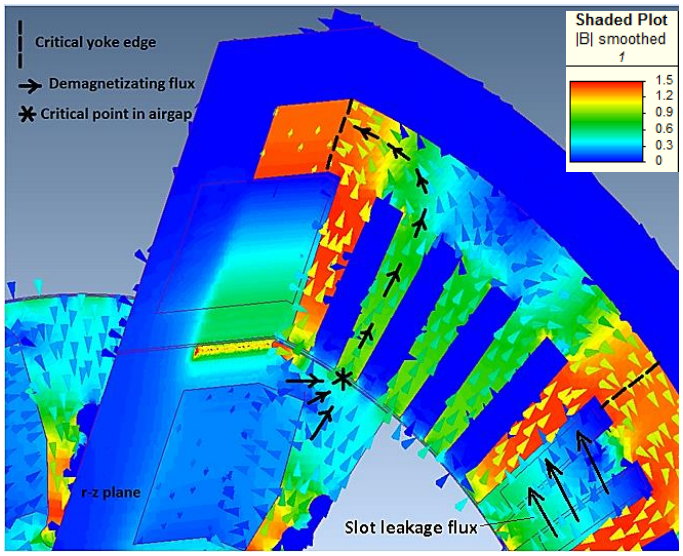

(a)

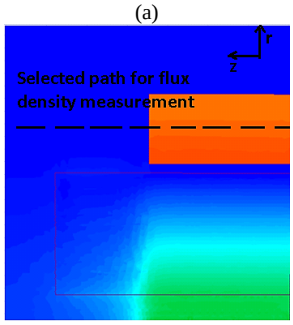

(b)

Fig. 3. 3D flux vector and flux density distribution in 39 mm stack model, under 160% I_{pk}. (a) Illustration of demagnetizing flux path and representative locations in airgap and yoke for flux density assessments. (b) Middle yoke selected path line for flux density assessments.

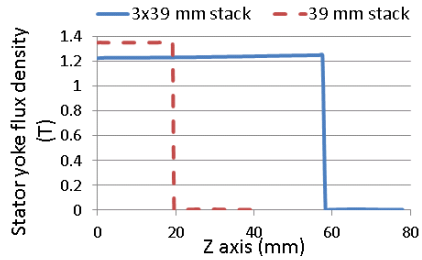

(a)

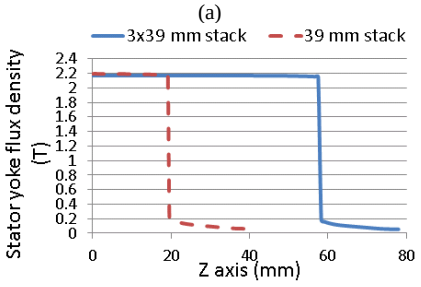

(b)

Fig.4. Representative flux density in the stator. (a) 160% I_{pk}. (b) 400% I_{pk}.

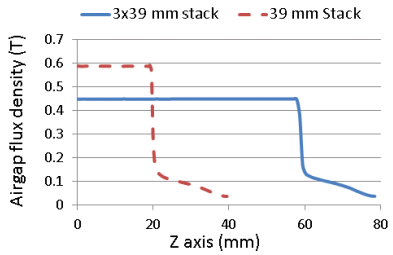

(a)

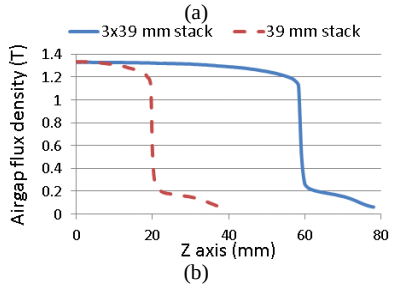

(b)

Fig.5. Representative flux density in the airgap. (a) 160% I_{pk}. (b) 400% I_{pk}.

B. Lumped circuit modelling

To explain the phenomenon in Fig. 2, a lumped magnetic circuit consisting of the armature reaction field and the magnets is proposed in Fig. 6. In this circuit, H_m corresponds to the field strength across the magnet, l_m is the width of the magnet along the magnetization direction, B_m corresponds to the operating flux density inside the magnet, A_m is the surface area of the magnet perpendicular to magnet flux, N is the number of turns in series, i is the armature current peak value, $R_{lamination}$ is the magnetic reluctance of the stator lamination observed by the armature field along the active stack length, $R_{end,\ arm}$ is the equivalent reluctance observed by the end winding field, R_δ is the airgap reluctance associated with the active stack length, $R_{PM,\ Internal}$ is the internal reluctance of the magnet, and $R_{leak,i}$, i=1,2,3 refer to the reluctance associated with magnet leakage through non-magnetic regions on top and bottom of the magnets, Fig. 1, [12], and the magnet leakage via the end faces. The reluctance parameters can be generally defined by (1), where l is the equivalent length of the flux traveling path, μ_r is the relative permeability of the material, and A is the surface area perpendicular to the traveling path of the flux.

$$R = l/\mu_0\,\mu_r A \tag{1}$$

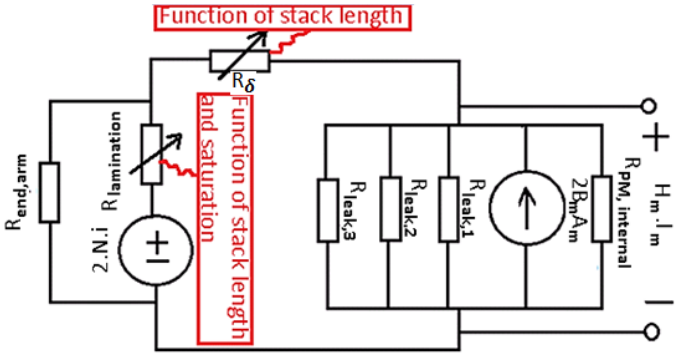

Fig. 6. Magnetic lump circuit for 3D modelling of demagnetization.

Treating the magnetic circuit and its parameters in Fig. 6 with an electrical analogy and using Ampere's Law the

equations (2) and (3) can be obtained. Replacing the B_δ (airgap flux density) in (3) by H_δ (airgap field) from (4), and replacing the H_δ in (2) by its extended form, the equation of the magnet load line can be obtained as (5), A_δ and l_δ corresponding to airgap reluctance parameters according to (1). It should be noted that in (5), α_0 and α_1 are the state of the art coefficients based on 2D modelling, while k_0 and k_1 are the additional 3D coefficients that account for the effects of the stack length and the magnetic saturation of the stator laminations.

By assigning appropriate values of length, area, and permeability into the reluctance equation, (1), the magnet load line in (5) can be obtained for different electromagnetic conditions. The following points proved critical in tuning the circuit parameters according to 3D FE results in Section III.A:

a) The appropriate permeability and equivalent lengths of the stator reluctance, required in (1), were imported from the 3D FE calculations.

b) The $R_{end,\ arm}$ is set to be independent from the stack length and about 34 times larger than the $R_{lamination}$; this ratio being based on the inverse of the end winding to magnetizing inductance ratio, which has been derived for the design with 195 mm stack.

c) It was realized that for the non-saturated conditions, the results from the lumped circuit modelling and the 3D FE simulations match more closely when the $R_{lamination}$ is replaced by $R_{lamination-modified}$ in (10), derived and explained in Appendix I.

$$2Ni.R_{end,arm}/\left(R_{end,leak}+R_{lamination}\right)=H_\delta l_\delta+H_m l_m \quad (2)$$
$$B_\delta A_\delta=2.B_m A_m(R_m/(R_m+R_\delta+R_s) \quad (3)$$
$$R_m=R_{PM,inetrnal}||R_{leak,1}||R_{leak,2}||R_{leak,3} \quad (3.1)$$
$$R_s=R_{end,arm}||R_{lamination} \quad (3.2)$$
$$H_\delta=B_\delta/\mu_0 \quad (4)$$
$$B_m=-k_0\alpha_0 H_m-2.k_1\alpha_1 N.i \quad (5)$$
$$\alpha_0=\mu_0.A_\delta.l_m/2A_m.l_\delta \quad (5.1)$$
$$\alpha_1=\mu_0.A_\delta/2A_m.l_\delta \quad (5.2)$$
$$k_0=(R_m+R_\delta+R_s)/R_m \quad (5.3)$$
$$k_1=k_0.R_{end,arm}/\left(R_{end,arm}+R_{lamination}\right) \quad (5.4)$$

Using equation (5), the magnet load lines for 39 mm and 195 mm stack lengths are calculated and compared in Fig. 7. The effect of magnetic saturation is assessed by comparing the short circuit currents with 160% I_{pk} and 400% I_{pk} amplitudes, and assigning appropriate permeabilities imported from the 3D FE simulations. The BH curve is the same as the one applied in Section III.A and belongs to the FB9B magnets at 20 ˚C.

As can be seen in Fig. 7, the magnet load line for the 400% I_{pk} and 195 mm stack length, intersects the non-linear part of the BH curve, indicating a partial demagnetization, confirming the 3D FE observation in Fig 2.(e). By reducing the stack length to 39 mm, the magnet load line is significantly shifted toward the linear section of BH curve, and the demagnetization risk is fully avoided with a large safety factor, again conforming to the 3D FE simulation results in Fig 2. (a). The major driving parameter behind the aforementioned shift of the magnet load line is the increase of the $R_{lamination}$ value relative to the $R_{end,\ arm}$ in (5.4), which is due to the reduction of A, (1) the flux path surface area, as a result of the reduced stack length, see Appendix II.

For the short circuit scenario with 160% I_{pk} , and 195 mm stack length, the magnet load line is already in a safe location on the linear part of the BH curve; however, shortening the stack length shifts the load line further inward and provides an even wider margin of safety against the demagnetization. The major driving parameter behind this phenomenon is the increase of the $R_{lamination-modified}$ value relative to the $R_{end,\ arm}$ in (5.4), which is due to the accelerated reduction of A, (1), as a result of the reduced stack length, and following the explanation given in Appendix I.

An interesting finding from the analysis in this section and Fig. 7 is that, although in scenarios with negligible magnetic saturation the demagnetization improvement via shortening the stack length might still be remarkable, the effect can be more significant and better appreciated for saturated designs and conditions. This is due to the lower permeability values of the stator laminations during saturated conditions, which narrows down the gap between $R_{lamination}$ and $R_{end,\ arm}$ values, thereby magnifying the impact of the stack length variation on k_1 in (5.4).

The essential part of the circuit in Fig. 6 can be summarized into the Magneto Motive Force (MMF) division between the active and non-active (end winding region) of the stator laminations. As shown in this chapter, taking this division into account (for both saturated and non-saturated conditions) may allow for a rapid and reliable assessment of the 3D demagnetization behavior when changing the motor stack length. Finally, it should be noted that the presented lumped model may, only, represent an overall, and approximate, level of demagnetization, i.e. (in contrast to FE simulations) it may not identify the local demagnetization effects in different regions of the magnet.

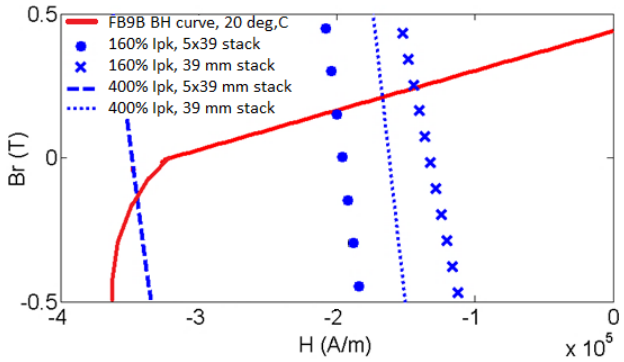

Fig. 7. Magnet BH curve and load lines for scenarios with different short circuit currents (accounting for saturation) and stack lengths.

IV. A Practical Application of the Concept

Based on the concept in section III, some practical applications within the field of electrical machines design can be imagined. For example, alongside with conventional 2D design methods in improving the demagnetization capability, shortening the stack length might result in considerable enhancement of demagnetization resistance and, therefore, such designs may benefit from cheaper grade of magnets with lower coercivities (this includes cheaper grade of ferrite

magnets, and the NdFeB magnets with lower Dy contents, [9]). To compensate for the reduced power due to the reduced stack length, the outer diameter of the machine can be increased. A first principle design practice on this basis and using extra weak Ceramic 8 magnets has been provided in Appendix III, where a same power level as a 195 mm stack design, with mitigated risk of demagnetization, has been achieved. To evaluate the effectiveness of the approach (i.e. stack length shortening) on better utilization of weak magnets and with a vision to demonstrate the concept via an existing prototype (which due to the shortened length may be viewed as a HEV rather than an EV traction design), the design in Fig. 1 is equipped with a cheaper but poorer grade of Ferrite magnet, Ceramic 8, which has about only 70% of the coercevity of the FB9B grade, see Table I. The performance of these two designs, in terms of demagnetization and the static torque, are simulated and compared in the following sections. Furthermore, the influence of changing the stack length on efficiency, power density, and power factor has been, separately, discussed in Appendix IV.

A. Demagnetization

The field strength across the Ceramic 8 magnets, under demagnetizing currents with amplitudes of 160%, 240% and 400% of the I_{pk} and comparing 39 mm and 195 mm stack lengths, has been simulated using FE 3D, and the results are shown in Fig. 8. The red and yellow areas correspond to the regions exposed to full or partial demagnetizations, respectively.

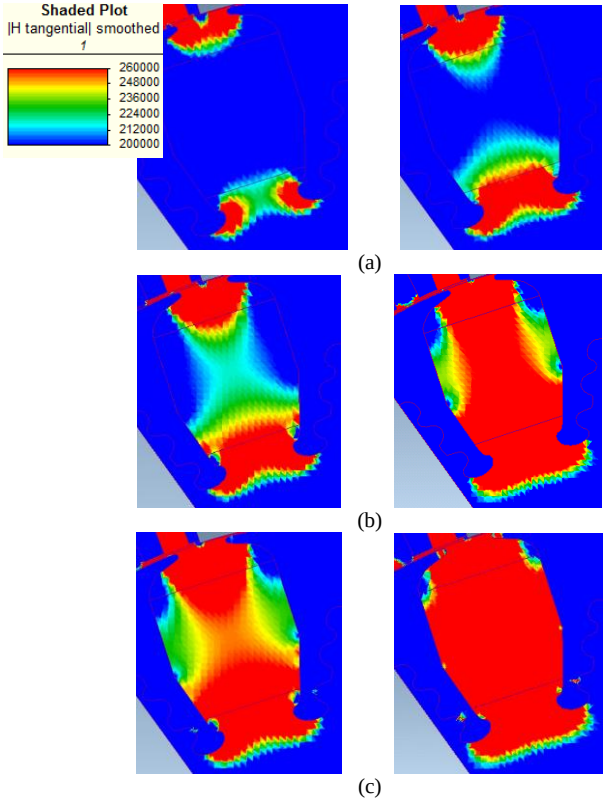

Fig. 8. Field strength distribution in the Ceramic 8 magnets, for designs with 195 mm stack length (right column), and 39 mm stack length (left column), and under negative d-axis currents with different amplitudes. (a) 160% I_{pk}. (b) 240% I_{pk}. (c) 400% I_{pk}. All results correspond to middle stack faces.

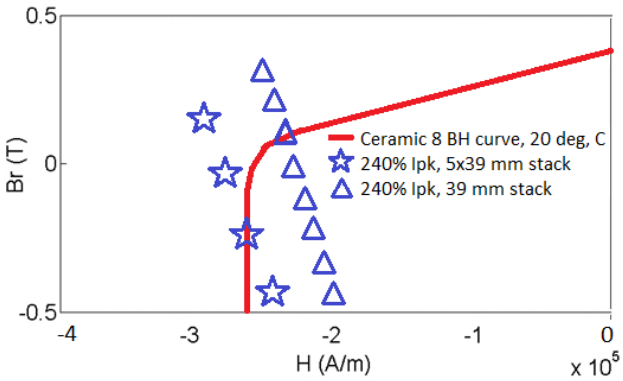

Fig. 9. Demagnetization assessment using the proposed lumped circuit model, Ceramic 8 magnets, 240% I_{pk}.

As seen in Fig. 8, following the proof of the concept in section III, the demagnetization performance is noticeably improved by shortening the stack length. Furthermore, confirming the explanation in Section III, the improvement factor is larger for the larger short circuit currents, which, in case of the model in Fig. 8, can be best observed for 240% I_{pk}, Fig. 8.(b), where the shortening of the stack length has reduced an 80% risk of demagnetization to less than 20% (the percentage is based on the demagnetized region divided by the full cross section of the magnet). The suitability of the lumped circuit model in Fig. 6 is assessed by investigating the Fig. 8(b) scenario, for which a good agreement with the FE 3D simulations has been achieved, Fig. 9.

B. Static Torque

To evaluate the power density of the 39 mm stack length design with Ceramic 8 magnets, the static torque of this design using both Ceramic 8 and FB9B magnet grades is simulated and compared using 3D FE, Fig. 10 (only 20% of the total electric loading is applied to match the prototype test set-up, Fig. 11(b)) . Comparing the peak torque values in Fig. 10 it can be realized that despite the 14% higher remanent flux density of the FB9B grade, it only contributes to 4% higher peak torque/ power density. This is majorly due to the saturation of the laminations at the peak torque operating point, and suggests that the use of weaker and cheaper grade of magnets might not, necessarily, compromise the peak torque and power density of the machine.

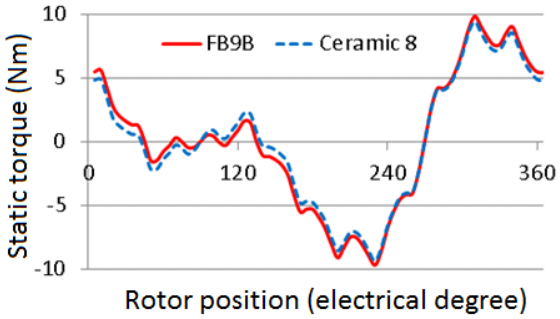

Fig. 10. Comparison of the static torque for the 39 mm stack length designs using FB9B and Ceramic 8 magnet grades.

V. Prototype Testing

To support the 3D FE tool and simulations in Section III, a prototype with 39 mm stack length corresponding to Fig. 1 and using both Ceramic 8 and FB9B Ferrite grades has been built and tested, Fig. 11. The rotor is once supplied by FB9B grade and once by Ceramic 8 grade magnets, and all tests are assured to be at the room temperature of 20 ˚C, which is identical to the assumed conditions in Sections III and IV. To simplify the manufacturing, only, two coils belonging to one of the phases have been wound, while the single phase current was adjusted to correspond to the 3-phase system, see Appendix V.

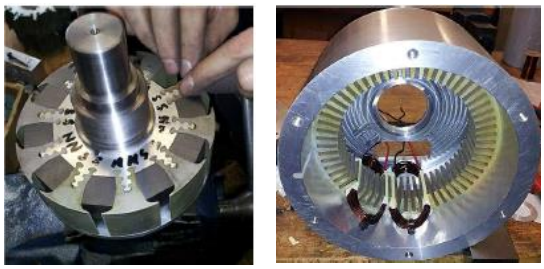

(a) (b)

Fig. 11. Prototype with 39 mm stack length. (a) Rotor. (b) Stator.

A. Demagnetization

To assess the demagnetization performance of the designs, currents with amplitudes of 160%, 240%, and 400% of the I_{pk} are injected in the negative d-axis position relative to the magnets. To have a more distinguishable result, each of the three current injections was targeted at only one magnet pole out of the ten, while it was assured that the three affected poles are distant from one another by, at least, one unaffected pole in between, [12].

After the current injections, the BEMF of the prototype has been measured for one full mechanical revolution, as shown in Fig. 12. In Fig. 12, only the distorted waveforms and the associated current levels are highlighted (160% I_{pk} for both magnet grades, and 240% I_{pk} in case of FB9B grade have not affected the BEMF waveforms).

To compare the results against the 3D FE findings in sections III and IV, the demagnetized regions in the FE models were replaced by air, and the BEMF of the modified models were re-calculated; the fundamental BEMF components from FE modelling and the prototype testing are compared in Figs. 13 and 14. From Figs. 13 and 14 it can be realized that: a) For both FB9B and Ceramic 8 magnets the prototype test results match closely with the 3D FE findings (compare the results for 39 mm stack length), confirming the validity of the FE tool and modelling applied in section III and IV; b) The largest variation of demagnetization performance due to change of stack length (indicated as margin of improvement in Figs. 13 and 14) has been obtained for the Ceramic 8 magnets, and for the case with 240% I_{pk} current. In this scenario, the stack length shortening mitigates the risk of demagnetization by 65%, which implies that the rather poor Ceramic 8 magnets may not only withstand the 3-phase short circuit currents (160% I_{pk}) with a good safety margin, but they can, also, retain much of their magnetic properties in case of more severe faults.

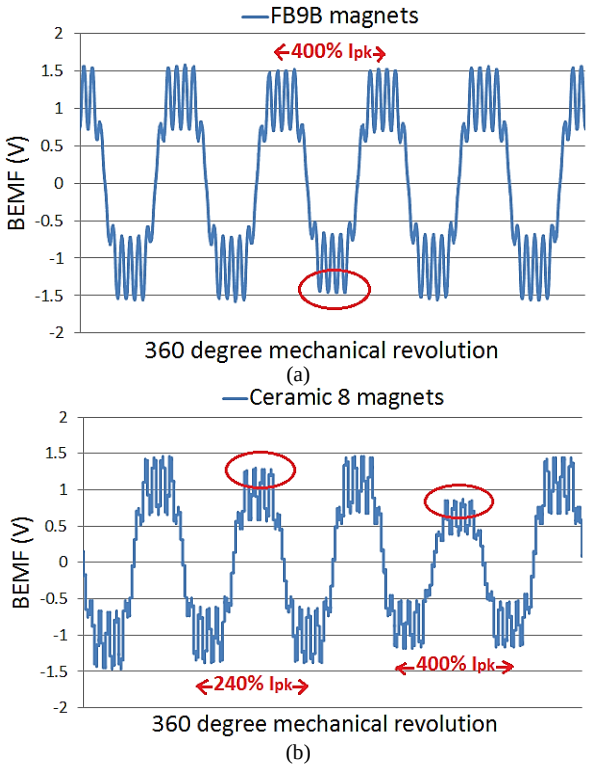

Fig. 12. BEMF waveforms after the demagnetization test. (a) FB9B. (b) Ceramic 8.

B. Static Torque

The static torque (measured at 100% I_{pk}) of the prototype with FB9B and Ceramic 8 magnets is measured and compared in Fig. 15 (only two coils out of the ten coils have been excited, Fig. 11(b) and Appendix II). Based on Fig. 15, the difference between the two magnet grades is about only 3% in peak torque, which matches well with the findings and explanation in Section IV.B. The 6% deviation between the simulation and the test results (Fig. 10 and Fig. 15) is partially due to the deviation of the actual materials characteristics from the data assumed in simulations, and partially due to the manufacturing tolerances which have been ignored in simulations.

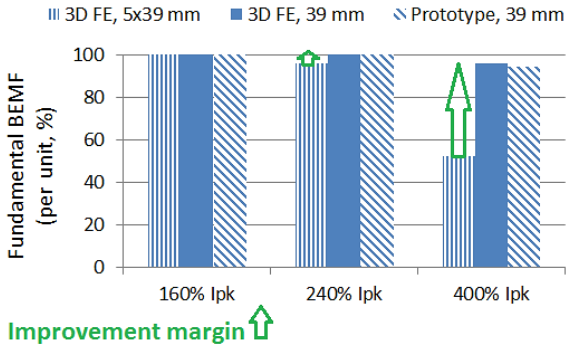

Fig. 13. Loss of BEMF fundamental component due to demagnetization, FB9B magnets

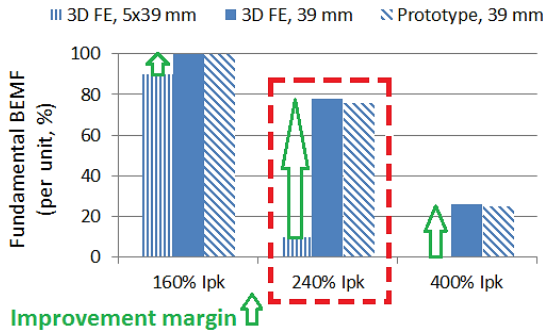

Fig. 14. Loss of BEMF fundamental component due to demagnetization, Ceramic 8 magnets.

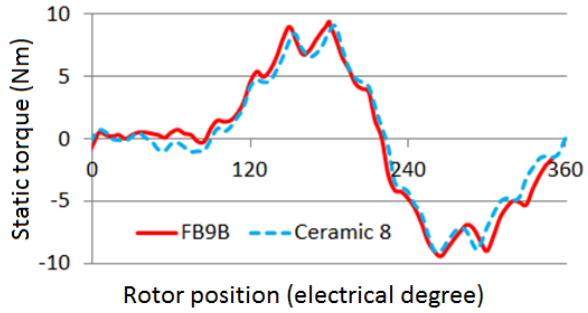

Fig. 15. Comparison of static torque test results for 39 mm stack length design using Ceramic 8 and FB9B magnets.

VI. Formulation of the 3D Concept and Modifying the State of the Art Equation

If the equation (5) is re-arranged with H_m as a function of B_m, an analytical expression to avoid the demagnetization risk can be obtained as in (6). In (6), the parameters γ and k_0 include the 3D effects from the stack length and magnetic saturation, while the other parameters, such as magnets width, number of turns and current amplitude are the state of the art parameters that are commonly used to mitigate demagnetization risk. The analytical expression (6) can be applied to enhance the conventional design optimization algorithms, while for most magnet grades, the B_{cj} (the magnet operating flux density corresponding to H_{cj}) can be approximated as zero.

$$\gamma . 2N . i/l_m + B_{cj}/k_0\alpha_0 < H_{cj} \quad (6)$$

$$\boldsymbol{\gamma = R_{end,leak}/(R_{end,leak} + R_{lamination})} \quad (6.1)$$

VII. Conclusion

This paper addressed the 3D demagnetization behavior of a ferrite based spoke type motor for an EV application. Based on a series of 3D FE simulations, analytical modelling, and prototype testing, it was shown that reducing the stack length might mitigate the demagnetization risk due to the increase of the stator laminations reluctance relative to the rather fixed end winding reluctance. Furthermore, it was shown that while the effect can be significant for the non-saturated conditions (due to an accelerated increase of the reluctance vs. stack length reduction), the effect might be, remarkably, pronounced for the saturated conditions due to the lower permeability of the laminations stack. The findings from the analyses have been summarized in a simple analytical expression, which can be applied to design optimization algorithms to mitigate demagnetization risks, and in particular to assist designing based on poorer and cheaper grade of magnets. This paper has revealed, explained and quantified the impact of the stack length on the demagnetization resistance of the embedded permanent magnet motors. Based on the findings, the cheap grade of magnets with poor demagnetization properties (such as low grade of ferrite magnets) may be better utilized in designs with larger diameter to stack length aspect ratio.

Acknowledgment

The authors gratefully acknowledge the support from Jaguar Land Rover under the Evoque-E project.

Appendix I

The variation of the flux density by shortening the stack length in Figs. 4 and 5 can be explained based on (7), (8), and (9), where the $R_{lamination}$ and $R_{end,leak}$ are the magnetic reluctance associated with the stator laminations stack and the end windings, respectively, φ and φ_{end} are the flux originated from the winding parts associated with the stack length and the end winding, respectively, Fig. 16(a), and A_0 is the flux path surface area associated with the stack length, l_z , Fig. 16(a). By shortening the stack length, and during non-saturated conditions, the $R_{lamination}$ and φ vary with a rate, which is equal or, as will be identified below, greater than the rate of the A_0 variation. As a result, the increase of the flux density in Figs. 4(a) and 5(a), may be attributed to the end winding flux flowing in the end regions of the laminations stack, φ_{end}, whose value is rather fixed and independent from the stack length variation, (9). An illustration of the φ and φ_{end} and the end stack region which is commonly engaged by the two, indicated as $l_{z,end}$, is given in Fig. 16(a). During saturated conditions, the unchanged values of the flux density against stack length variation, suggests that either $R_{lamination}$ and φ vary with a greater proportion compared to the non-saturated conditions or φ_{end}, unlike the non-saturated conditions, is not fixed and decreases with shortening of the stack length.

Due to the linear and non-saturated conditions of the laminations material (in case of the low demagnetizing currents), and to improve the lumped circuit modelling in Section III.B, the φ and φ_{end} , in Fig. 16(a), can be separated assuming each one occupies a distinct fraction of the laminations stack volume, as illustrated in Fig. 16(b), where $0 < \beta < 1$. As a result of this modelling, it can be realized that the $R_{lamination}$ experiences a smaller effective surface area than A_0 , and may be, more accurately, expressed as (10). Following the explanation above and based on (10), it can be realized that during non-saturated conditions, the $R_{lamination-modified}$ changes with a greater rate than the stack length variation.

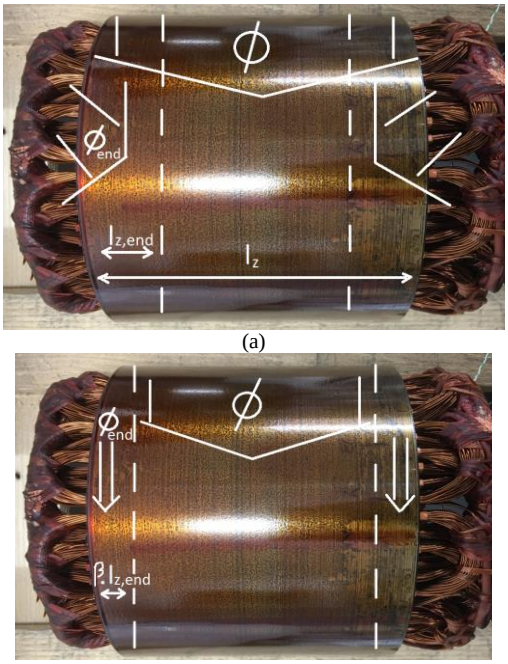

Fig. 16. Illustration of the reduced effective surface area for the demagnetizing field/ flux. (a) Actual model. (b) Equivalent model.

$$\varphi = 2Ni/R_{lamination} \quad (7)$$

$$\varphi_{end} = 2Ni/R_{end,leak} \quad (8)$$

$$B = (\varphi + \varphi_{end})/A_0 \quad (9)$$

$$R_{lamination-modified} \propto 1/(l_z - \beta . l_{z,end}) \quad (10)$$

APPENDIX II

Decomposing the axial flux, due to the end windings effect, by implementing the equivalent model explained in Fig. 16(b), it can be realized that the flux associated with the stack length, φ, travels a radial path through the stator teeth and a circumferential path through the stator yoke region, as illustrated in Fig. 17 (a 39 mm against a 2 x 39 m stack have been compared). Please note that in Fig. 17, φ, only, corresponds to the demagnetization flux (field is a better term to use, but flux is more illustrative), and the leakage flux which does not link the rotor magnets, and only contributes to the magnetic saturation in the $r - \emptyset$ plane (i.e. the plane perpendicular to the axis of rotation) has not been included.

From the illustration in Fig. 17, it can be realized that changing the stack length does not affect the length of the demagnetization flux path (illustrated as l1+l2+l3 in Fig. 17), whereas the cross section perpendicular to the flux path (illustrated as A_t for the cross section in the tooth, and A_y for the cross section in the yoke) changes linearly with the stack length variation. On this basis, and from (1), it is clear that the reluctance associated with the stator laminations, $R_{lamination}$ has a direct and reverse proportion to the stack length variation.

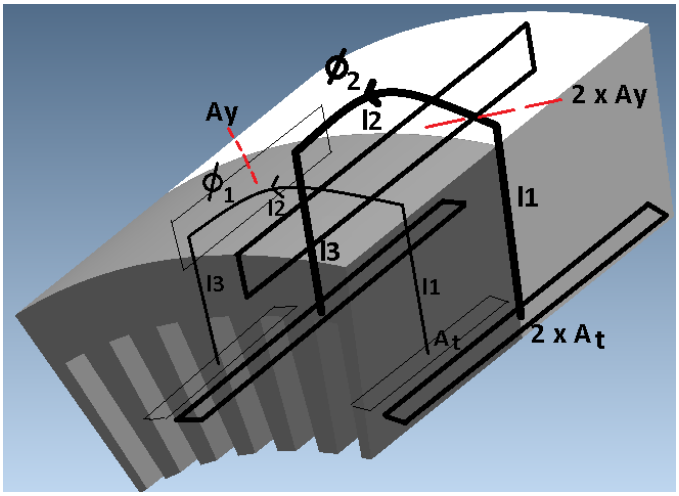

Fig.17. Illustration of the variation of stator laminations reluctance by varying (halving) the stack length.

APPENDIX III

To demonstrate the feasibility of a high power design using extra weak ferrite magnets (ceramic 8), a first principle design was made by, simply, scaling the dimeter and length of the original design in Tables 1 and 2. To assess the effect of shortening the length and decompose it from other parameters such as pole number, etc, same pole number, as well as electric and magnetic loading was maintained during the scaling. The design outcome is shown in Fig. 18(a), where the demagnetization capability under a 240% I_{pk} fault, and for two different stack lengths, has been simulated following a similar 3D FE set up in Section III. As shown in Figs. 18(b) and (c), the design with short stack length demonstrates a, significantly, stronger demagnetization withstand capability, making the use of the extra weak ferrite magnets feasible for a demanding high power density application. Based on a basic comparison of the performance and cost of the high power ceramic 8 design and the FB9B ferrite design, Table III, it can be realized that following a simple size scaling, a reduction of magnet cost using an extra cheap grade magnet is feasible, but the cost effect is partially negated due to the additional winding mass, as the length of the end windings was kept unchanged during the scaling. Finally, with regards to the exploitation of cheaper grade magnet materials the following comments should be noted:

a) While in this paper, the comparisons are, only, made between two different grades of ferrite magnets, the same principles are applicable and should be practiced for NdFeB grades with high and low contents of dysprosium. It is expected that due to the much higher price range of the NdFeB grades, the suitability of the concept in terms of reducing the demagnetization risk, and therefore enabling the, significantly, cheaper designs using low content dysprosium magnets will become more evident.

b) Based on the studies in this paper, reducing the stack length for a motor with distributed winding design is proved to be an effective parameter, which together with other approaches such as maximizing the number of poles, magnet burial in the rotor core, etc can contribute to enhancing the demagnetization performance of the weak and extra weak NdFeB or ferrite grade magnets, enabling such cheap material

being used for low cost but high performance traction motor applications. The degree of merit of this exploitability might differ depending on the application and requirements. However, based on the information and guidelines provide in this paper, the designers may assess and, depending on the level of merit, utilize the concept for their specific design targets.

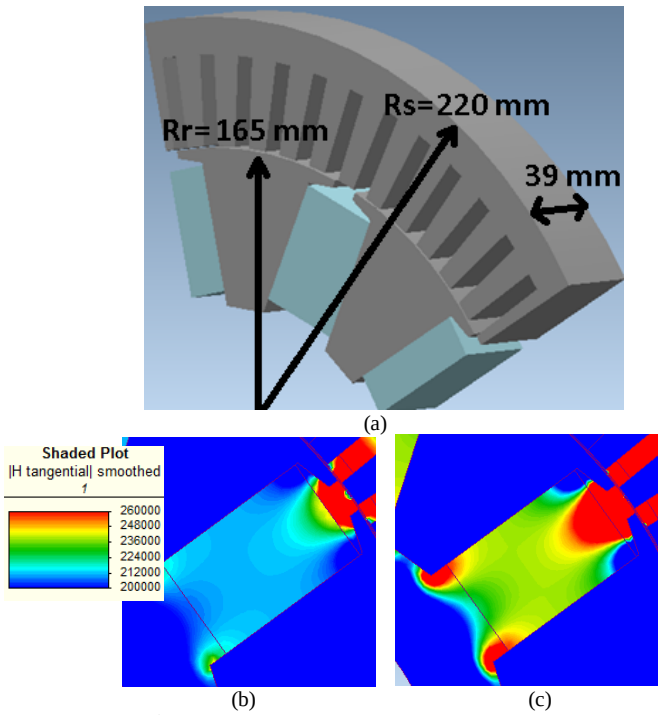

Fig. 18. 80 kW first principle design using ceramic 8 magnets, and scaled diameter. (a) Topology and geometry. (b) Demagnetization field for design with 39 mm stack, 240% $I_{pk.}$ (c) Demagnetization field for design with 2 x 39 mm stack, 240% $I_{pk.}$

TABLE III
First principle performance and cost assessment of the EV motor design using ceramic 8 ferrite magnets.

	FB9B magnets	Ceramic 8 magnets
Peak torque-Peak power	260 Nm-~80 kW	260 Nm-~80 kW
Motor volume (per unit)	1	1
Active material mass (per unit)	1	1.2
Magnets mass (kg)	4	4
Magnets cost (per unit)	1	0.7

APPENDIX IV

The efficiency map of the designs with 195 mm and 39 mm stack length, and FB9B magnets have been calculated using FE 2D , and accounting, only, for the winding (only DC loss) and iron loss parts, and shown in Fig. 19. The 3D effect of stack length has been taken into account by including the end windings resistance and inductance, as well as reducing the available DC link voltage by the same factor as the stack length change, i.e. 5. From Fig. 19, it is realized that by shortening the stack length the efficiency has dropped by about 1% in the key operating points (i.e. the points at which the vehicle runs most frequently) and more significantly in the high torque-low speed regions; the efficiency fall is, majorly, due to the increase of the per unit end winding resistance in the case of design with shorter stack length. Furthermore, based on Fig. 18, by shortening the stack length the base speed of the design (thereby the power density) is reduced, this being, majorly, due to the larger per unit end winding inductance for a fixed available per unit DC link voltage.

Following a similar procedure, the effect of reducing the stack length on power factor was investigated in FE 2D and by including the end winding resistance and inductance. Based on the results, the influence of the stack length was realized to be negligible throughout the operating range.

Finally, it should be noted that as the shortening of the motor stack length (to improve demagnetization performance) may be followed by increasing the motor diameter (to enhance the torque and power output), a re-optimization of the motor design with respect to power density, efficiency, and power factor might become necessary, which is outside the scope of this paper.

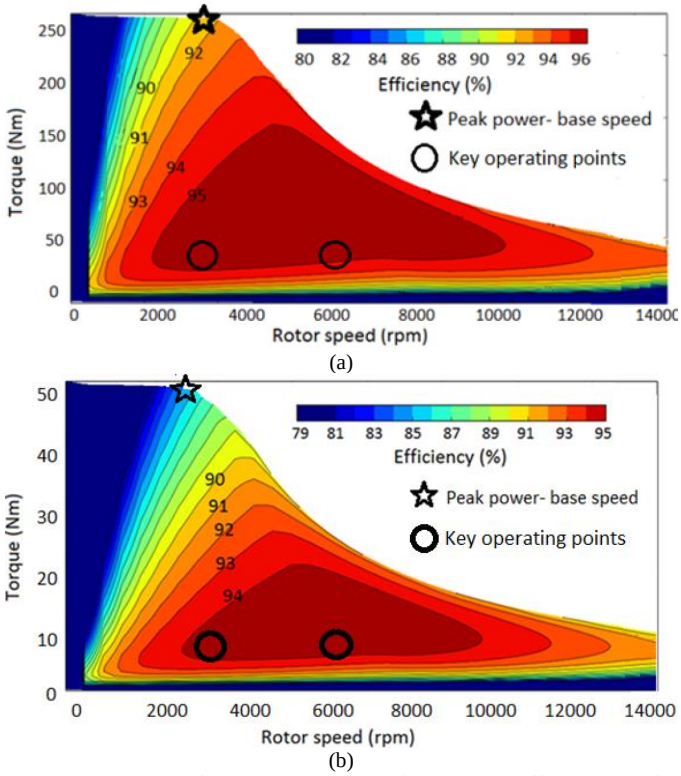

Fig. 19. Comparison of peak torque-speed performance and efficiency map for 195 mm stack length and 39 mm stack designs with FB9B.

APPENDIX V

It can be shown that for a balanced 3-phase system, with sinusoidal distribution of MMF in time and space, the 3-phase MMF is 1.5 times that of the associated 1-phase MMF, [22]. Using FE, and by taking the effects from the additional harmonics into account, it is realized that, for the present motor design with 2 slots per pole and phase and the given particular stator and rotor topology, the static torque and demagnetization performance of the 3-phase system can be approximated by a 1-phase system with 1.25 times the actual 3-phase current, Figs. 20 and 21, and (11).

$$I_{pk-1\,phase} \approx 1.25\,.\; I_{pk-3\,phase} \qquad (11)$$

Based on the aforementioned transformation of 3-phase to 1-phase system, (11), and to simplify the prototype manufacturing, the full 3-phase overlapping windings have been reduced to only two non-overlapping coils belonging to one of the phases, Fig. 11(b). As a result, to match the theoretical analysis to the prototype test set up, while obtaining an equivalent 3-phase system performance, throughout this paper I_{pk} refers to $I_{pk-1\,phase}$, (11).

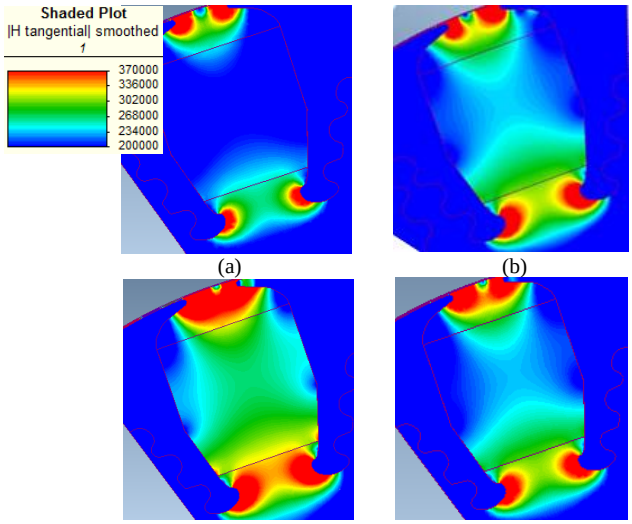

Fig. 20. Comparison of the demagnetization behavior under 1-phase and 3-phase system excitations, FE 2D, FB9B magnets. (a) 100% Ipk in 1-phase system. (b) 100% Ipk in 3- phase, Ib=Ic=-0.5 Ia. (c) 150% Ipk in 1-phase system. (d) 125% Ipk in 1-phase system.

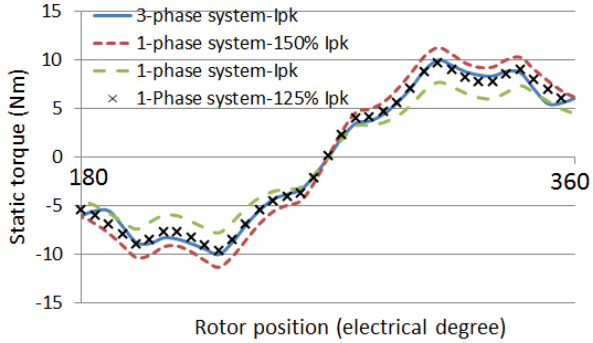

Fig. 21. Comparison of the static torque under 1-phase and 3-phase system excitations.

REFERENCES

[1] J. D. Santiago, H. Bernhoff, B. Ekergårdet, *et al*., "Electrical Motor Drivelines in Commercial All Electric Vehicles: a Review,'' IEEE Trans. Vehicular. Tech., vol. 61, no. 2, pp 475-484, Feb. 2012.

[2] T. A. Burress, S. L. Campbell, C. L. Coomer, *et al*., "Evaluation of the 2010 Toyota Prius Hybrid Synergy Drive System,'' Oak Ridge Nat. Lab., Oak Ridge, TN, USA, ORNL/TM-2010/253, Mar. 2011.

[3] R. H. Staunton, T.A. Burress, and L.D. Marlino, "Evaluation of 2005 Honda Accord Hybrid Electric Drive System,'' Oak Ridge Nat. Lab., Oak Ridge, TN, USA, ORNL/TM-2006/535, Sep. 2006.

[4] Y. Sato, S. Ishikawa, T. Okubo, *et al*., "Development of High Response Motor and Inverter System for the Nissan leaf electric Vehicle,'' SAE Technical Paper 2011-01-0350, Apr. 2011.

[5] W. L. Soong and N. Ertugrul, "Field-Weakening Performance of Interior Permanent-Magnet Motors," IEEE Trans. Ind. Appl., vol. 38, no. 5, pp. 1251-1258, Sep/Oct. 2002.

[6] A. Sarikhani, and O. A. Mohammed, "Demagnetization Control for Reliable Flux Weakening Control in PM Synchronous Machine," IEEE Trans. Energy. Convers., vol. 27, no. 4, pp. 1046-1055, Dec. 2012.

[7] B. A. Welchko, T. M. Jahns, W. L. Soong, and J. M. Nagashima, "IPM Synchronous Machine Drive Response to Symmetrical and Asymmetrical Short Circuit Faults, " IEEE Trans. Energy. Convers., vol. 18, no. 2, pp. 291-298, June. 2003.

[8] I. Boldea, L. N. Tutelea, L. Parsa, and D. Dorrell, "Automotive electric propulsion systems with reduced or no permanent magnets: An overview," IEEE Trans. Ind. Electron., vol. 61, no. 10, pp. 5696–5711, Oct. 2014.

[9] S. J. Galioto, P. B. Reddy, A. M. EL-Refaie, "Effect of Magnet Types on Performance of High Speed Spoke Interior Permanent Magnet Machines Designed for Traction Applications,'' in *Proc. IEEE ECCE*, Sep. 2014, pp. 4513 - 4522.

[10] S. Morimoto, S. Ooi, Y. Inoue, and M. Sanada, "Experimental Evaluation of a Rare-Earth-Free PMASynRM with Ferrite Magnets for Automotive Applications,'' IEEE Trans. Ind. Electron., vol. 61, no. 10, pp. 5749 – 5756, Oct. 2014.

[11] D. G. Dorrell, M. F. Hsieh, and A. M. Knight, "Alternative rotor designs for high performance brushless permanent magnet machines for hybrid electric vehicles," IEEE Trans. Magn., vol. 48, no. 2, pp. 835–838, Feb. 2012.

[12] M. Kimiabeigi, J. D. Widmer, R. Long, Y. Gao, J. Goss, R. Martin, T. Lisle, J.M. Soler Vizan, A. Michaelides, and B. Mecrow, "High Performance Low Cost Electric Motor for Electric Vehicles Using Ferrite Magnets," IEEE Trans. Ind. Electron., vol. 63, no. 1, pp. 113-122, Jan. 2016.

[13] J. A. Farooq, A. Djerdir, and A. Miraoui, "Analytical Modeling Approach to Detect Magnet Defects in Permanent-Magnet Brushless Motors," IEEE Trans. Magn., vol. 44, no. 12, pp.4599–4604, Dec. 2008.

[14] K. C. Kim, K. Kim, H. J. Kim, and J. Lee, "Demagnetization analysis of permanent magnets according to rotor types of interior permanent magnet synchronous motor," IEEE Trans. Magn., vol. 45, no. 6, pp. 2799–2802, Jun. 2009.

[15] B. N. Cassimere, S. D. Sudhoff, and D. H. Sudhoff, "Analytical Design Model for Surface-Mounted Permanent-Magnet Synchronous Machines," IEEE Trans. Energy. Convers., vol. 24, no. 2, pp. 347-357, June. 2009.

[16] J. J. Potgieter, and M. J. Kamper, "Calculation Methods and Effects of End-Winding Inductance and Permanent-Magnet End Flux on Performance Prediction of Nonoverlap Winding Permanent-Magnet Machines," IEEE Trans. Ind. Appl., vol. 50, no. 4, pp. 2458-2466, July/Aug. 2014.

[17] A. Youmssi, "A three-dimensional semi-analytical study of the magnetic field excitation in a radial surface permanent-magnet synchronous motor," IEEE Trans. Magn., vol. 42, no. 12, pp. 3832–3841, Dec. 2006.

[18] Z. Q. Zhu, Y. Pang, D. Howe, *et al*.,"Analysis of Electromagnetic Performance of Flux-Switching Permanent-Magnet Machines by Nonlinear Adaptive Lumped Parameter Magnetic Circuit Model," IEEE Trans. Magn., vol. 41, no. 11, pp. 4277–4287, Nov. 2005.

[19] J. Pyrhönen, V. Ruuskanen, J. Nerg, J. Puranen, and H. Jussila, "Permanent-Magnet Length Effects in AC Machines," IEEE Trans. Magn., vol. 46, no. 10, pp.3783–3789, Oct. 2010.

[20] M. Kimiabeigi, J. D. Widmer, R. Long, Y. Gao, J. Goss, R. Martin, T. Lisle, J.M. Soler Vizan, A. Michaelides, and B. Mecrow, "On Selection of Rotor Support Material for a Ferrite Magnet Spoke Type Traction Motor," early access publication in IEEE Trans. Ind. Appl., Feb 2016.

[21] J. D. Widmer, R. Martin, and M. Kimiabeigi, "Electric vehicle traction motors without rare earth magnets," Sustainable Materials and Technologies (Elsevier), Feb 2015.

[22] Sadarangani C., 2000, "Electrical machines – Design and analysis of induction and permanent magnet motors", KTH, Stockholm, Sweden, ISBN 91-7170-627-5, ISSN 1404-8248, August.